Heliyon 9 (2023) e21702

Contents lists available at ScienceDirect

Heliyon

journal homepage: www.cell.com/heliyon

A_2LiGaI_6 (A = Cs, Rb): New lead-free and direct bandgap halide double perovskites for IR application

Anwar ul Haq [a], Tasawer Shahzad Ahmad [b], Afaq Ahmad [c], Badriah S. Almutairi [d], Muhammad Amin [a], M.I. Khan [a,*], Nimra Ehsan [e], Ramesh Sharma [f]

[a] Department of Physics, The University of Lahore, 53700, Pakistan
[b] Department of Physics, University of Okara, Pakistan
[c] Centre of Excellence in Solid State Physics, University of the Punjab, Lahore, Pakistan
[d] Department of Physics, College of Science, Princess Nourah bint Abdulrahman University, P.O.Box 84428, Riyadh, 11671, Saudi Arabia
[e] Department of Chemistry, The University of Lahore, 53700, Pakistan
[f] Deptment of Applied Science, Feroze Gandhi Institute of Engineering and Technology, Raebareli, 229001, Uttarpradesh, India

ARTICLE INFO

Keywords:
Optical properties
Photoelectric
Solar cell
Density functional theory
TB-mBJ
Double-perovskite
Lead-free

ABSTRACT

Recently, all inorganic double perovskites have drawn a lot of interest as promising solar materials. The optical, structural, thermoelectric, electronic, and mechanical properties of double halide perovskites A_2LiGaI_6 (A = Cs, Rb) are explored via first-principles calculations with the WIEN2k code, using GGA PBEsol and TB-mBJ potentials. The majority of perovskite materials utilized in the highest-performing solar cells have bandgaps ranging between 1.48 and 1.62 eV. The compounds A_2LiGaI_6 (A = Cs, Rb) have a direct bandgap of 1.51 eV and 1.55 eV, respectively, and are expected to be useful in solar cells. The optical study shows that there are large absorption bands in the visible region, as determined by the dielectric constant, absorption, and other dependent factors. Their potential for use in solar cells is increased by their absorption in the visible part. The BoltzTraP code has been used to perform thermoelectric studies to assess the electrical, thermal conductivities, and Seebeck coefficient. They are important for construction of thermoelectric generators that harvest heat energy because of their high figure of merit and incredibly low thermal conductivity of lattice at ambient temperature. Furthermore, by examining the spectroscopic limit maximum efficiency, up to 30 % efficiency is predicted for both compositions, which paves the way for the applicability of them in solar energy conversion.

1. Introduction

Nearly 85 % of the world's population relies on limited fossil fuels for energy, which has negative effects on the environment and people's health. Furthermore, until 2050, energy consumption will be doubled. Sustainable energy sources such as hydro, wind, and solar energy are becoming important [1]. As a result, researchers are working hard to develop solar cells with higher efficiency. Perovskite solar cells (PSCs) are rapidly becoming the most advanced due to their low-price and high-power conversion efficiency (PCE). We are all aware that the photovoltaic technology that is advancing the quickest in terms of development and research PSCs. Beginning with a dye-sensitized solar cell, researchers employed the hybrid inorganic-organic halide perovskite (HIOHP) $CH_3NH_3PbI_3$

* Corresponding author.
E-mail address: muhammad.iftikhar@phys.uol.edu.pk (M.I. Khan).

https://doi.org/10.1016/j.heliyon.2023.e21702
Received 7 March 2023; Received in revised form 18 October 2023; Accepted 26 October 2023
Available online 30 October 2023
2405-8440/© 2023 Published by Elsevier Ltd. This is an open access article under the CC BY-NC-ND license (http://creativecommons.org/licenses/by-nc-nd/4.0/).

as a light-sensitizer to achieve a PCE of 3.8% [2]. Hybrid perovskites such as $NH(CH_3)_3SnX_3$ (X = Br, Cl) [1], ABI_3 (A = NH_2CHNH_2, CH_3NH_3; B═Pb, Sn) [3], and $CH_3NH_3PbI_3$ have been noted as a possible replacement for high-efficiency solar cells [4]. The PCE of hybrid perovskites is relatively high: it is larger than 19 % in most cases [5,6]. Pb halide perovskite (HP)-based solution processed solar cells have already attained a record-breaking efficiency of over 22 % in a single-junction arrangement [7]. The extraordinary device efficency is due to the remarkable optical and electrical features of lead (Pb)-based perovskite, including their small bandgap with significant optical absorption coefficient, extended carrier lifetime, stable charge carriers transport, and low exciton binding energy [8,9]. Lead-based perovskites are toxic, not environmentally friendly, and deteriorate under a variety of conditions, including visible and ultraviolet light, heat, water vapour pressure, applied electric field, ambient air, and mechanical pressure. This is one of the main reasons why they are not a popular source of sustainable light-to-electricity conversion [10–13].

Finding stable and Pb-free substitutes with comparable optoelectronic capabilities to Pb-based perovskites is one of the intrinsic remedy to solve these problems [14–20]. This technique necessitates extensive searches through enormous compositional and structural areas, which would be too time-consuming and costly for standard trial-and-error experiments [21]. As a result, computational initiatives are required to design and discover efficient lead halide perovskite alternatives. The inorganic halide perovskites, also known as double perovskites, are highly sought-after for study due to their successful use as light-absorbing materials in photovoltaic devices [16,17].

Two significant substances, Cs_2LiYBr_6 and Cs_2LiYI_6 are also members of the family of crystalline elpasolite materials and are currently referred to as double perovskite lead-free halides [18,19]. These double perovskites halides, notably Cs_2LiYX_6 (where X = Cl and Br), are said to have a stable cubic phase (space-group: $Fm\overline{3}m$). Existing literature includes experimental evidence that supports this. Additionally, it has been documented in the literature that crystals from this family exhibit good scintillation characteristics when excited by gamma radiation. As a result, light yield during the scintillation process is said to be freed in the energy range of 20,000–70, 000 ph/MeV. The energy resolution of $Cs_2LiLaBr_6$ at 662 keV is 2.9 %.

The fact that these materials involve d-f transitions as a result of the existence of the trivalent cationic sites with perfect O_h symmetry in the rare earth elements makes them extremely fascinating as well. Furthermore, it has been shown that Li-containing lead-free double perovskites halides can transform incident neutrons into secondary ionizing particles; as a result, these halides are thought to be promising for neutron and gamma-ray scintillator detectors with cerium (Ce) doping. Additionally, these materials are of particular interest for their luminescence properties due to the presence of core valence electrons. For instance, Loef et al. investigated the spectroscopic and scintillation property of both the pure and cerium doped Cs_2LiYX_6 (X = Br, Cl) and, as a consequence, they got novel information on the Ce doped and pure Cs_2LiYX_6 (X = Cl, Br), and examined their scintillation mechanism [20]. Eijk et al. studied the role of thermal neutrons scintillator with elpasolite Cs_2LiYBr_6, in addition to the decay timings and light yields from the monoclinic crystalline substance Li_3YBr_6 that contains Ce doping. With 1 % doping of Ce in CsLiYBr, a high value of light-yield of 64,000 x $\frac{photons}{thermal\ neutron}$ was demonstrated from Cs_2LiYBr_6: Ce. The other, however, displayed an 88,200 photon yield per thermal neutron. Interestingly, both Cs_2LiYX_6 compounds (X = Br, I) share the same crystal structure, allowing us to study the anion influence specifically on optical characteristics [19–21].

Using the WIEN2k code for energy applications, we developed the materials A_2LiGaI_6 (A = Cs, Rb) based on an analysis of the aforementioned literature and the energy demand. The amount of literature on this significant compound is extremely limited. To describe how materials are used in sustainable devices, a thorough grasp of material qualities are necessary. In order to achieve this, density functional theory (DFT) simulations with Tran-Blaha modified Becke-Johnson (TB-mBJ) potential have been used to assess the electronic structures, refraction, absorbance coefficient, and dielectric constants of the double perovskites A_2LiGaI_6 (A = Cs, Rb) [22–29]. The use of the TBmBJ potential has significantly improved the accuracy of bandgap calculations for semiconductors compared to previous methods. While the GW approximation still offers the highest level of accuracy, its computationally intensive nature makes the TBmBJ potential an appealing option for researchers and practitioners who value a balance between precision and computational efficiency. In summary, the TBmBJ potential provides a notable advancement in accurately estimating semiconductor bandgaps, presenting a valuable alternative to the GW approximation in terms of accuracy and computational considerations [22,23,27,30]. In addition to the thermal and electrical conductivities, figure of merit and Seebeck coefficient of the transport properties have been examined. To carry out experimental research for fabricating solar cells and thermoelectric generators, our theoretical analysis of A_2LiGaI_6 (A = Cs, Rb) compound will supply the knowledge and trends needed to understand optoelectronic and thermoelectric properties.

2. Computational details

In this communication, to explore the required characteristics of the present crystalline materials, a computational program called WIEN2k based on full-potential augmented plane waves (APW) and local orbitals (lo) has been utilized [24,25,27]. Using an exchange-correlation functional PBEsol [24], the structural optimization at ground state and elastic properties of crystals were computed. An additional functional TB-mBJ was employed to investigate optoelectronic properties [26–31]. Within the interstitial zone and muffin tin spheres, electronic systems' spherical harmonic and plane wave solutions were taken into consideration [31]. Initial parameter values for the cutoff energy, the Gaussian parameter Gmax, the angular momentum l, and RKmax in reciprocal lattice are −0.7 mRy, 12, 10 and 8 respectively. We set the energy and charges convergence criterion to be 0.01 mRy and 0.0001e, respectively.

Thermoelectric parameters such as thermal conductivity (κ), electrical conductivity (σ), seebeck coefficient (S), power factor (PF), and the electronic component of the figure of merit (ZTe) were computed.

$$\frac{\sigma}{\tau} = \frac{ne^2}{m^*} \tag{1}$$

equation (1) describes the relationship between electrical conductivity (σ) and variables such as electric charge (e), charge density (n), and effective mass (m*). The relationship between temperature and σ can be explained using the subsequent formula [32–34].

$$\sigma(T,\mu) = \frac{1}{\Omega}\int \sigma_{\alpha\beta}(\epsilon)\left[\frac{-\partial f_0(T,\mu,\epsilon)}{\partial\epsilon}\right]\partial\epsilon \tag{2}$$

Equation (2) mathematically explains the relationship between temperature and electrical conductivity (σ) using the transport energy distribution tensor represented by $\boldsymbol{\sigma}_{\boldsymbol{\alpha}\beta}$ (∈), with $\boldsymbol{\alpha}$ being the indices of the energy distribution tensor. The chemical potential is denoted by $\boldsymbol{\mu}$, and Ω is the volume of unit cell. Thermal conductivity (κ) is the transfer of heat energy due to temperature differences and consists of two components: electronic conductivity (κe) and lattice conductivity (κl). This parameter is composed of two components: the κ_e, which is due to electronic transport, and the k_l, which is caused by lattice vibrations (phonons).

$$k = k_e + k_l \tag{3}$$

The thermo-power (S) calculated through equation (3), represented the voltage generated in response to a temperature gradient, where its mathematical formula that we used is of the form [34].

$$S(T,\mu) = \frac{1}{eT\Omega\sigma_{\alpha\beta}(T,\mu)}\int \sigma_{\alpha\beta}(\epsilon)(\epsilon-\mu)\left[\frac{-\partial f_0(T,\mu,\epsilon)}{\partial\epsilon}\right]\partial\epsilon \tag{4}$$

The integral in equation (4) involves the product of the energy (ϵ) minus the chemical potential ($\boldsymbol{\mu}$) and the partial derivative of the Fermi-Dirac distribution function (f_0) with respect to energy (ϵ). Equation (5) gives power factor (PF) which is another crucial thermoelectric parameter that determines the effectiveness of a thermoelectric device. It can be expressed mathematically as:

$$PF = S^2\sigma \tag{5}$$

A dimensionless number that represents the conversion efficiency of thermoelectric materials is called the figure of merit (ZT) and computed with equation (6). The following relatin can be used to compute it [11,32–34].

$$ZT = \frac{S^2\sigma\, T}{k} \tag{6}$$

3. Result and discussions

3.1. Structural properties

With the composition of A_2LiGaI_6 (A = Cs, Rb), the Wyckoff locations of the A location at (¼, ¼, ¼) and (¾, ¾, ¾), Li at

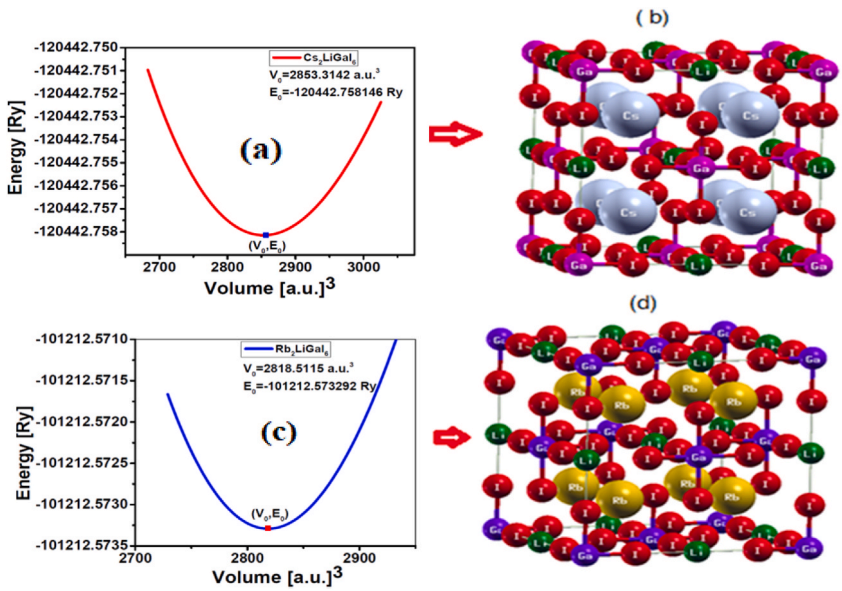

Fig. 1. (a) Optimized plot of Cs_2LiGaI_6 (b) Crystal Structure of Cs_2LiGaI_6 (c) Optimized plot of Rb_2LiGaI_6 and (d) Crystal Structure Rb_2LiGaI_6.

(½,0,0), Ga at (0,0,0), and I at site (x, 0,0) are shown in Fig. 1(b, d) [23,30,31]. Moreover, calculations based on generalized gradient approximation with the PBE for solids (GGA-PBEsol) calculations reveal that the lattice parameters of Cs_2LiGaI_6 and Rb_2LiGaI_6 are 11.9144 Å and 11.8807 Å, correspondingly with space group 225 (Fm $\overline{3}m$). The material's stability is an essential aspect of ensuring the device's performance. The tolerance, octahydral and modified tolerance factors for two A_2LiGaI_6 (A = Cs, Rb) perovskite materials to forecasting structural stability have been estimated through equaions (7–9) respectively. The Goldschmidt tolerance factor is a measure of crystal structure stability and distortion. The following

Relationsips and their respective ionic radii are used to derive these variables:

$$\tau = \frac{r_A + r_X}{\sqrt{2}(r|B + r_X)} \tag{7}$$

$$\mu = \frac{r_B}{r_X} \tag{8}$$

$$\tau = \frac{r_X}{r_B} - n_A \left[n_A - \frac{\frac{r_A}{r_B}}{ln\left(\frac{r_A}{r_B}\right)} \right] \tag{9}$$

where r_A, r_X are Cesium/Rubidium, halogen atom Radii respectively and r_B is the mean radii of the locations B^+, B^{+3} [30,31]. Table 1 enlisted the estimated values of octahedral, tolerance and modified tolerance factors. Fig. 1(a,c) display the energy vs. volume

Optimization plots that were created using the Birch-Murnaghan equation of state equation (10) as follows:

$$E(v) = E_0 + \frac{9B_0V_0}{16}\left\{\left(\left(\frac{V_0}{V}\right)^{\frac{2}{3}} - 1\right)B_0' + \left(6 - 4\left(\frac{V_0}{V}\right)^{\frac{2}{3}}\right)\left(\left(\frac{V_0}{V}\right)^{\frac{2}{3}} - 1\right)^2\right\} \tag{10}$$

3.2. Electronic properties

Fig. 2 (a and b) show the estimated band structures of two Cs/Rb-based perovskites. For the present perovkite materials, both the valence band maxima (VBM) and conduction band minima (CBM) are found at the same high symmetry point at (Γ- Γ). The calculated bandgaps of two perovskites are given in Table 1. The calculated direct bandgaps of Cs_2LiGaI_6 and Rb_2LiGaI_6 in the visible range are 1.51 eV and 1.55 eV, correspondingly, highlighting their importance for solar and optoelectronic systems. The density of states (DOS) is important physical parameter for comprehending the electronic characteristics of materials. Fig. 3(a and b) illustrate the partial density of states (PDOS) and total density of states (TDOS) for A_2LiGaI_6 (A = Cs and Rb) using TB-mBJ-GGA approximations. The 5p orbital of halogen I dominate the valence band top of A_2LiGaI_6, while 4p-Ga, 5p-I, and 2s-Li states dominate the conduction band bottom of A_2LiGaI_6 (A = Rb and Cs) halide Perovskites. The inter-band transition electrons are controlled by the states of 4p-Ga and 5p-I, with Ga-4p states being the first conduction zone in all compounds. For Rb_2LiGaI_6 and Cs_2LiGaI_6, the s-Rb and s-Cs states are.

Accountable for the e^- being free in the structure. Only valence electrons are capable of hybridization and inter-band transitions, and when carriers acquire energy, electrons go directly from the valence to the conduction bands.

3.3. Mechanical properties

Although the examined alloys have cubic symmetry, we have computed just three independent elastic parameters symbolized as C_{44}, C_{12}, and C_{11}, which are shown in Table 2, to characterize all mechanical properties. The results show that the elastic constants are positive, and the accuracy of the calculations that follow is checked using the Born criterion given in equation (11) for the cubic model [35–40].

$$C_{11} > 0; C_{44} > 0; C_{11} - C_{12} > 0; C_{11} + 2C_{12} > 0; C_{12} < B < C_{11} \tag{11}$$

The following formulas given in eqations (12–16) are used to compute the Young, bulk, shear moduli. Higher shear, Young, and bulk Modulus indicated a high resistance to deformation.

Table 1
The estimated lattice parameters, tolerance factors and bandgap E_g at ground state energy.

Parameters	Cs_2LiGaI_6	Rb_2LiGaI_6
Lattice parameter Å	11.9144	11.8807
Bandgap (eV)	1.51(*direct*)	1.55(*direct*)
Tolerance factor (t)	0.8152	0.9021
Octahedral factor (μ)	0.9318	0.9318
Modified Tolerance factor (τ)	4.5970	3.1584

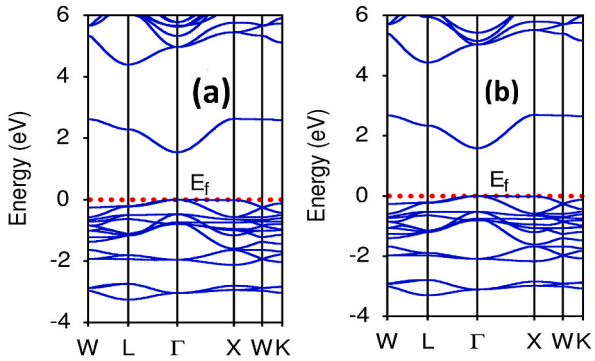

Fig. 2. Graphs illustrating total density of states and band structure for (a) Cs_2LiGaI_6 and (b) Rb_2LiGaI_6.

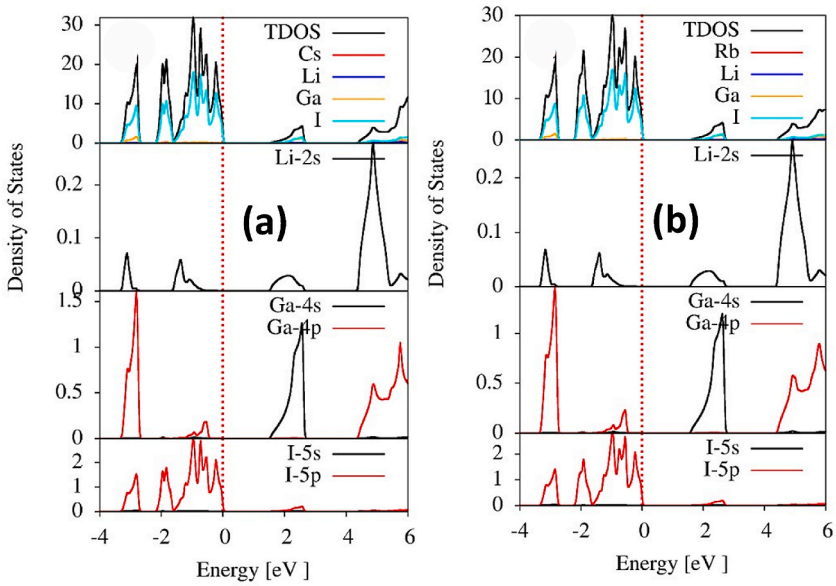

Fig. 3. PDOS of (a) Cs_2LiGaI_6 and (b) Rb_2LiGaI_6.

Table 2
Elastic parameters(C_{44}, C_{12}, C_{11}), shear modulus S, bulk modulus B, Young modulus Y, anisotropic constant A, Cauchy's pressure C_P, Pugh ratio B/S, Poisson's ratio, and shear constant C' for Cs_2LiGaI_6 and Rb_2LiGaI_6.

Parameters	C_{11} (GPa)	C_{12} (GPa)	C_{44} (GPa)	B (GPa)	S (GPa)	Y (GPa)	B/S	ν	A	C_P	C'
Cs_2LiGaI_6	38.6662	8.5715	10.5161	18.6031	12.1424	25.3824	1.532	0.232	0.690	−1.945	15.047
Rb_2LiGaI_6	28.5622	7.2738	7.8059	14.3699	8.8395	18.8063	1.626	0.245	0.733	−0.532	10.644

$$B = \frac{(C_{11} + 2C_{12})}{3} \tag{12}$$

$$S = \frac{(S_V + S_R)}{2} \tag{13}$$

$$S_V = \frac{(C_{11} - C_{12} + 3C_{44})}{5} \tag{14}$$

$$S_R = \frac{5(C_{11} - C_{12})C_{44}}{3(C_{11} - C_{12}) + 4C_{44}} \tag{15}$$

$$Y = \frac{9BS}{3B + 2S} \tag{16}$$

due to plasticity and amplified strength of the materials. The brittleness and ductility of materials are measured using Pugh's ratio (B/S), Poisson's ratio given in equation (17), and Cauchy's pressure in equation (18). If ($v > 0.26$, $B/S > 1.75$, and $C_P > 0$) [36–40], the material is ductile; otherwise, it is brittle. Our named compounds' computed Pugh's and Poisson's ratios, as well as Cauchy's pressure, are less than the limit values; thus, our studied compounds are brittle.

$$\nu = \frac{3B - 2S}{2(3B + S)} \tag{17}$$

$$C_P = C_{12} - C_{44} \tag{18}$$

$$C' = (C_{11}\text{-}C_{12}) / 2 \tag{19}$$

The shear constant computed by using equation (19). The shear constant's + ve value C' stands for the dynamical stability of the material [40]. Our designated compositions have positive shear constant values, demonstrating their dynamic stability. The anisotropic Zener factor A determined by equation (20) that indicates whether the substance is anisotropic or isotropic, where it is represented as [39,40].

$$A = \frac{2C_{44}}{C_{11} - C_{12}} \tag{20}$$

The material is isotropic when A = 1, whereas it becomes anisotropic when A deviates from unity. Due to the varying values of A from unity, our named compounds are anisotropic materials.

3.4. Optical properties

The way a substance interacts with light is referred to as its optical characteristics. When designing solar cells, it's essential to understand how the material used will respond to different frequencies of light, as this can have a significant effect on the solar cell's efficiency. The behavior of material properties like conductivity, reflection, and absorption with the interaction of light is very important in designing solar cells. The dielectric function $\varepsilon(\omega)$ is the most essential parameter to understand optical characteristics, where it is represented as: $\varepsilon(\omega) = \varepsilon_1(\omega) + i\varepsilon_2(\omega)$. In this case, $\varepsilon_1(\omega)$ and $\varepsilon_2(\omega)$ are the dielectric function's real and imaginary portions. The real portion $\varepsilon_1(\omega)$ is attained using the Kramers Kronig relations using equation (21), and the imaginary portion $\varepsilon_2(\omega)$ is found via summing all unoccupied to occupy interband transitions given in equation (22) [41,42].

$$\varepsilon_1(\omega) = 1 + \frac{2P}{\pi} \int_0^\infty \frac{\omega' \varepsilon_2(\omega)}{\omega'^2 - \omega^2} d\omega \tag{21}$$

$$\varepsilon_2(\omega) = \frac{h' e^2}{\pi m^2 \omega^2} \sum_{ij} \int |M_{cv}(k)|^2 \delta(\omega_{cv}(k) - \omega) d^3k \tag{22}$$

The optical transitions are estimated using the dipole matrix $M_{cv} = < \varphi_{ck} \vee e\nabla \vee \varphi_{vk} >.$, where m and e are the mass and charge of electron, respectively, and ω is the angular frequency of EM radiation. The real component of the dielectric constant $\varepsilon_1(\omega)$, is the measurement of the material's capacity to polarize in the presence of electric field at a particular frequency (ω). This property determines how much light is reflected or transmitted by the material, which affects the overall efficacy of the solar cell. The dielectric constant's imaginary part, $\varepsilon_2(\omega)$, is an estimate ability of the material to absorb light at a particular frequency (ω). The quantum particle transitions from valence to conduction bands when maximum energy of light may interact with the material, and this causes the appearance of the peaks in $\varepsilon_2(\omega)$. That is, we can say that the electron may transit from their ground state in the valence band to higher energy levels in the conduction band when maximum energy of light interacts with the material. In our case, we obtain two peaks in $\varepsilon_2(\omega)$; one corresponds to visible and other corresponds to UV radiation of light. With the use of the $\varepsilon_1(\omega)$ and $\varepsilon_2(\omega)$ dielectric functions, all other key optical characteristics such as refractive index $n(\omega)$, extinction $k(\omega)$ and absorption coefficients $\alpha(\omega)$, conductivity $\sigma(\omega)$ and reflectivity $R(\omega)$ can be calculated through equations 23–26 respectively [42–45].

$$n(\omega) = \frac{1}{\sqrt{2}} \sqrt{\left(\sqrt{\varepsilon_1(\omega)^2 + \varepsilon_2(\omega)^2} + \varepsilon_1(\omega) \right)} \tag{23}$$

$$k(\omega) = \frac{1}{\sqrt{2}} \sqrt{\left(\sqrt{\varepsilon_1(\omega)^2 + \varepsilon_2(\omega)^2} - \varepsilon_1(\omega) \right)} \tag{24}$$

$$\alpha(\omega) = \frac{\sqrt{2}\omega}{c}\sqrt{\left(\sqrt{\varepsilon_1(\omega)^2 + \varepsilon_2(\omega)^2} - \varepsilon_1(\omega)\right)} \tag{25}$$

$$R(\omega) = \left|\frac{\sqrt{\varepsilon(\omega)} - 1}{\sqrt{\varepsilon(\omega)} + 1}\right|^2 \tag{26}$$

Utilising TB-mBJ exchange potentials, all of these optical characteristics were investigated [41,42]. Fig. 4(a) and (b) show the dielectric function's real and imaginary parts. For energies of (2.1, 2.8) eV for Cs_2LaGaI_6 and (2.2, 2.85) eV for Rb_2LiGaI_6, the imaginary and real components of the dielectric show their first peak at the resonance frequency. The peaks swiftly decline to the minimal value after resonance. These measurements have a relationship to the visible region, making them useful in the solar sector. The static dielectric constant of Cs_2LiGaI_6 (3.45) is greater than the static dielectric constant of Rb_2LiGaI_6 (3.3), as shown in Fig. 4(a). Penn's model, confirms that the bandgap of Cs_2LiGaI_6 is less than that of Rb_2LiGaI_6. When $\varepsilon_1(\omega)$ has negative values, the material exhibits a metallic nature. As the metallicity of a compound increases, so does its reflectivity, thus the maximum reflectivity is observed in the range where $\varepsilon_1(\omega)$ is negative. Fig. 4c and d represent the refractive index and imaginary part k(ω) which is essentially an energy function in eV. Phase velocity in an EM is measured as the real component of n(ω). The influence of the moving EM wave in the same medium is regulated by the k(ω). The static refractive index for both materials, index $n(0) = \sqrt{\varepsilon_1(0)}$, is calculated up to 1.85. For Cs_2LiGaI_6, the n(ω) and k(ω) values are measured to be 5.0 eV and 7.0 eV, correspondingly, which

Changed to 5.2 and 7.5 eV the change of composition Rb_2LiGaI_6. The ability of a material or medium to absorb electromagnetic radiation is measured by the absorption coefficient. It is defined as the ratio of the absorbed energy to the incident energy per unit distance traveled by the radiation or wave through the material. Similarly, conductivity is the degree of a material's capability to conduct electric current and is related to the imaginary component of the dielectric constant. A higher conductivity leads to a lower loss of energy due to resistance in the solar cell. Fig. 5(a and b) illustrate the\ absorption coefficient and conductivity, which are essential material properties. Cs_2LiGaI_6 and Rb_2LiGaI_6 have their initial maximum absorption band and conductivity peaks in the visible energy band 2.8 eV–3.0 eV and 2.65 eV–2.8 eV, correspondingly. This further supports the validity of these materials in solar industry. In the lower energy range, the reflectivity increases from Rb to Cs, as illustrated in Fig. 5(c). Fig. 5(d) shows the eloss function, which shows the decline in light energy within the material. At 3eV, the greatest eloss was detected.

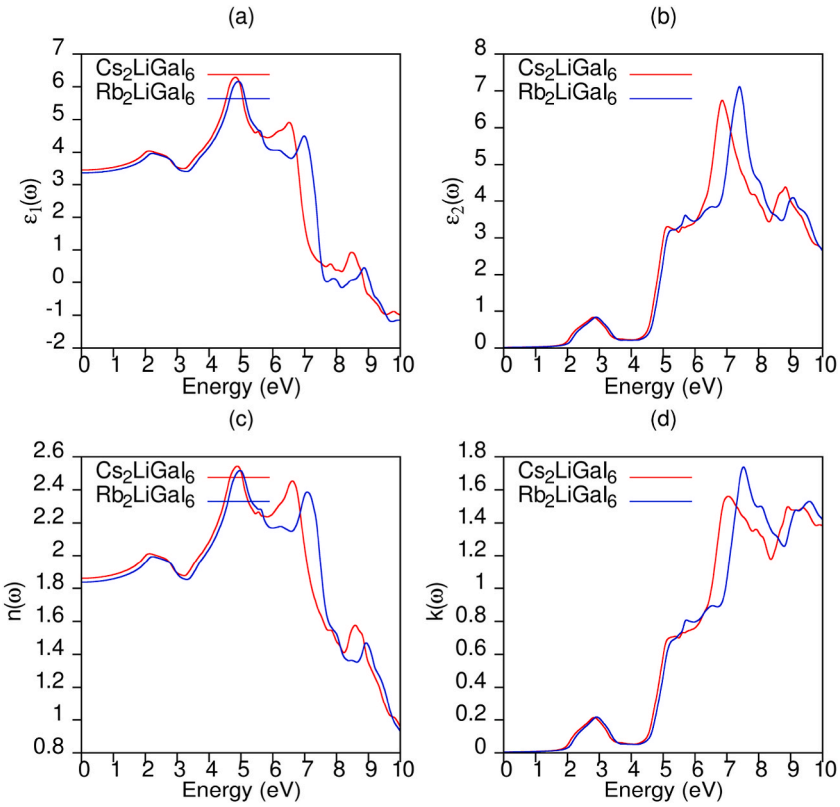

Fig. 4. (a) Real dielectric constant, (b) imaginary dielectric constant, (c) refractive index, and (d) extinction coefficient.

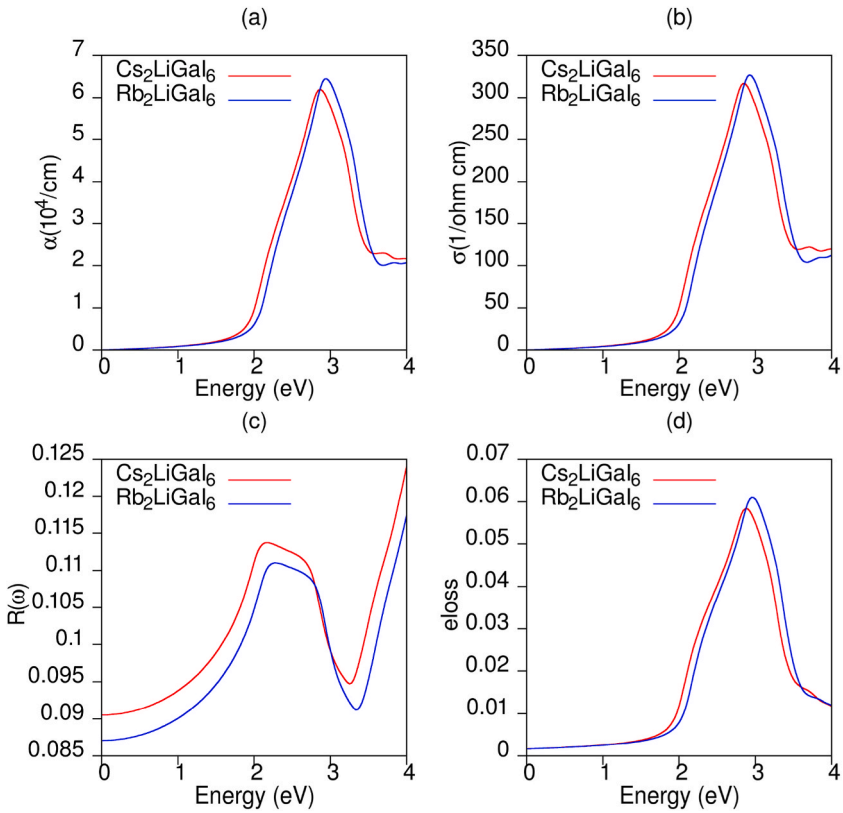

Fig. 5. (a) Absorption coefficient (b) conductivity (c) reflectivity, and (d) eloss.

3.5. Transport properties

By using the BoltzTraP code, the thermoelectric characeristics of Rb_2LiGaI_6 and Cs_2LiGaI_6 are investigated. Calculations are used to estimate the characteristics of the materials in relation with σ, k, and S. The ZT is determined by the thermoelectric material efficiency measurement formula $ZT = \frac{\sigma S^2}{K} T$ [38,39]. The material can have a higher thermoelectric efficiency if it has a large σ and a low k. The k is composed of ke, and k_l, where $k = k_e + k_l$ [41,42]. Figs. 6 and 7 show the computed transport characteristics in terms of T(k) and μ(eV). Fig. 6 (a, b) illustrates how the presence of n or p-types of charges carriers relie on the +ive or -ive value of μ(eV). In the BoltzTraP code, tt is utilized throughout this work's calculations, relaxation time (τ), which has a fixed value ($\tau = 10^{14}$s), was utilized to divide the variables σ and k. Rb_2LiGaI_6 and Cs_2LiGaI_6 have maximum σ values at 300k of 9.2/Ω-m and 7.5/Ω-m, respectively, in the p-type area from −0.15 eV to zero energy. For Rb_2LiGaI_6 and Cs_2LiGaI_6, the σ remains negligible for the n-type region. Based on these findings, we deduce that the cation changes from Cs to Rb when the σ rises. For Rb_2LiGaI_6 and Cs_2LiGaI_6, the values of σ rises from 0.01/0.02 1/Ω-m (50K) to 1.5/1.45 1/Ω-m (1200K) as seen in Fig. 6 (c). This is a result of temperature-related bond breakage, which results in emission of more electrons together with the increment of their energy. coulomb repulsion causes the change in σ from Rb to Cs to be less [46–49]. The bandgap's value has a significant impact on the 'S'. Metals have a low value of 'S', while insulators have a high 'S' value. Therefore, the Seebeck coefficient would be less and vice versa depending on how wide the band gap was. On the other hand, conductivity varies in direct proportion to the effective charge carried [47,48]. Thermal conduction in a material is generated by the movement of electrons and phonons. In our analysis, we considered the electronic part of thermal conductivity due to the limitations of the classical Boltzmann transport theory-based BoltzTraP code. In Fig. 6(d,e,f), we present the plot between the thermal conductivity (k_e) against the chemical potential as well as temperature ranging from 50 K to 1200 K. As temperature increases, k_e also rises due to the increased occurrence of thermal collisions resulting from the larger ionic radius of I. Within the p-type region, the highest peaks of thermal conductivity are observed within the range of −0.5 to −1.0 eV.

The seebeck coefficient (S) is depicted in Fig. 7(a, b, and c) as a function of chemical potential (μ-E_F) at various temperatures (200 K, 400K, 600 K, 800 K, 1000K and 1200K). The Seebeck coefficient exhibits sharp peaks and dips for the full range of chemical potential. Positive and negative potentials both have high-intensity maxima at 300 K, and when the temperature rises to 600 and 800 K, these values start to fall. Since bound electrons are energized via gaining thermal energy and produce pairs of electrons and holes, the character is diminishing. Because the bands are small and dispersed with the prohibited region near the Fermi level and fewer charge carriers are present in this range, the most noticeable peaks are of 0–1 eV. S's highest possible value at 300 K, the maximum values of S for Rb_2LiGaI_6 and Cs_2LiGaI_6, respectively, are 2700 μV/K and 2500 μV/K. It is clear from comparing the outcomes of these two

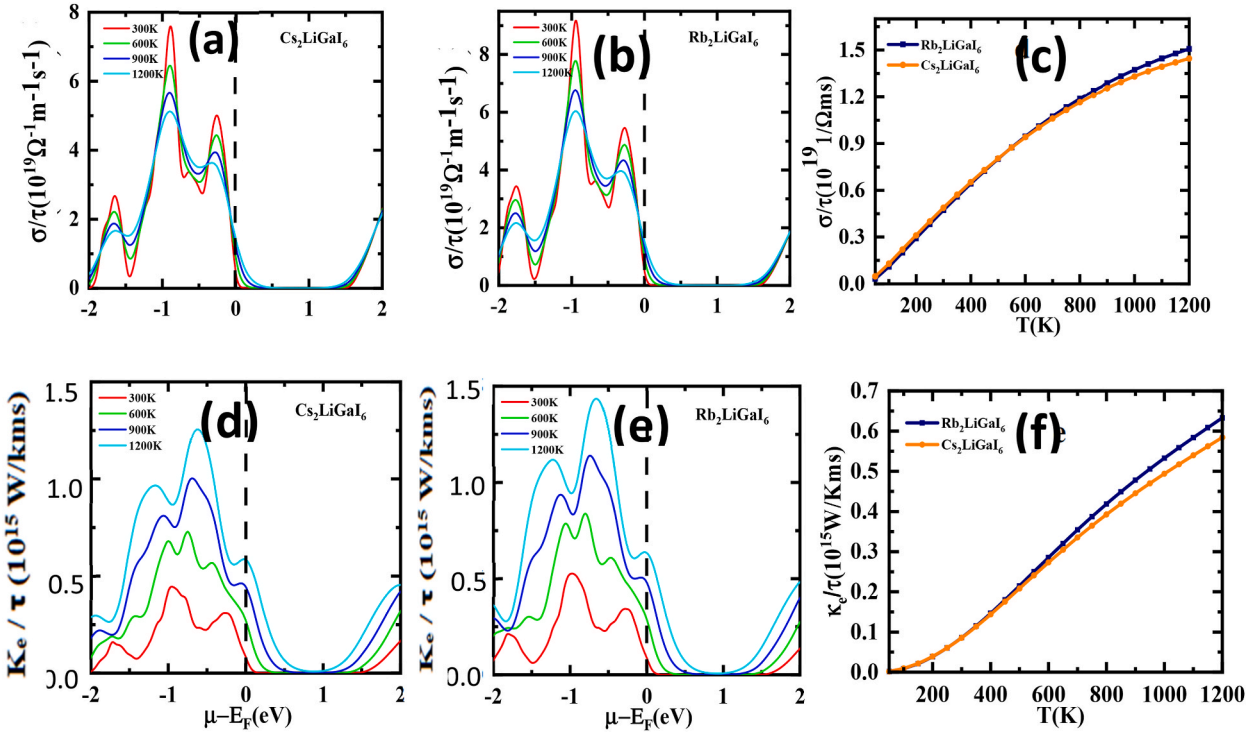

Fig. 6. (a, b, c) Electrical conductivity (σ) (d, e, f) Thermal conductivity (k) of Rb2LiGaI6 and Cs2LiGaI6 calculated as function of μ-EF(eV) and T(k).

compounds that Rb_2LiGaI_6 exhibits a higher Seebeck coefficient due to the existence of a bigger bandgap. The observed outcomes are quite consistent with related other materials results calculated theoretically that have already been published, validating our findings [46–51].

Fig. 7(d,e,f) depicts the power factor (PF) calculated versus chemical potentials and temperatures ranging from 50 K to 1200 K. The PF exhibits a linear growth pattern until it reaches 800 K, reaching a value of 4×10^{10} W/K^{2}ms for Rb_2LiGaI_6 and 3.8×10^{10} W/K^{2}ms for Cs_2LiGaI_6. The significantly higher PF values make these perovskite systems particularly suitable for high-temperature thermoelectric applications. The dimensionless ZT is the most significant factor that evaluates the effectiveness of thermoelectric materials. The relationship between ZT and σ and the coefficient of Seebeck clearly shows that ZT rises but falls with an increase in thermal conductivity. The values of ZT for Cs_2LiGaI_6 and Rb_2LiGaI_6 in terms of the chemical potential at temperatures of 1200 K, 1000 K, 800 K, 600 K and 300 K are shown in Fig. 7(g, h,i). These two halide perovskites feature distinct peaks, the highest of which has a ZT that is almost equal to 1. The fact that these materials are semiconductors explains the high value of ZT. The graph shows that the magnitude of ZT starts to increase as the temperature increases and touches its highest value at high temperature.

3.6. *Spectroscopic limited maximum efficiency*

The spectroscopic limited maximum efficiency (SLME) model, which uses an ideal diode circuit and AM1.5G and DFT computed absorption spectra as two key input factors, is an effective technique for estimating theoretical PCEs of solar cells [52]. SLME is the extended form of Schockley-Queisser (SQ) limiting efficiency. SLME approach, based on Fermi golden rule, is important to design highly efficient devices as compared to the SQ limit. SLME is used to measure the maximum efficacy of the photovoltaic materials by taking into account the absorptivity a(E), thickness of the materials L, bandgap values and radiative/non-radiative recombination losses. We determined the absorptivity from the following relation equation (27):

$$a(E) = 1 - e^{2\alpha(E)L} \tag{27}$$

where α(E) is absorption coefficient obtained from first principle and L is thickness of the materials. The AM1.5G solar spectrum data is also used as input for SLME calculations [53].

Using direct bandgap and theoretical absorbance coefficients, the SLME of investigated materials has been calculated to be 30 % efficient at 26 °C. However, we have found that their conversion efficiency as light harvesting devices have a substantial amount of space for improvement. Theoretical details of SLME calculations are reported in Fig. 8.

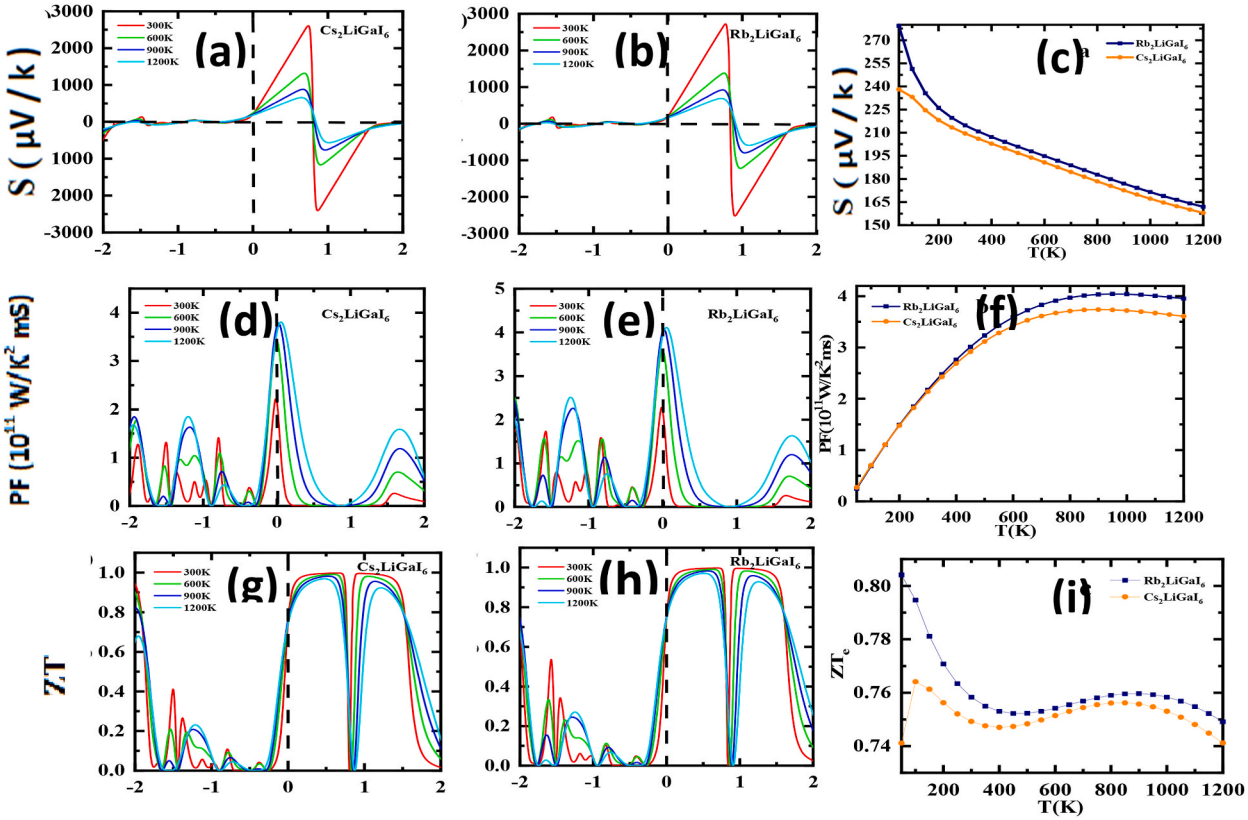

Fig. 7. (a, b,c) Seebeck coefficient, (d, e, f) power factor, and (g, h,i) figure of merit of Cs_2LiGaI_6 and Rb_2LiGaI_6.

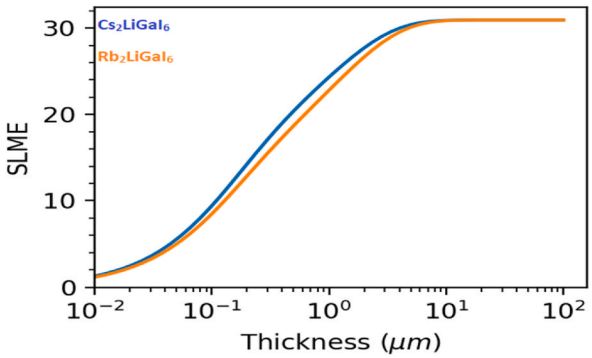

Fig. 8. SLME calculated at room temperature for the two double perovskites A_2LiGaI_6, where A = Cs, Rb.

4. Conclusion

In brief concluding remarks, the elastic, structural, transport and optoelectronic characteristics of cubic halide perovskites A_2LiGaI_6 (where A = Rb and Cs) were analyzed through a broad DFT study using WIEN2k code. The optimized lattice constants of these Ga-based materials are calculated at 0 K temperature, which have no experimental data available yet. It is likely to have a cubic structure for A_2LiGaI_6 (where A = Rb and Cs) at ground state with space group# 225 (Fm $\overline{3}m$). The structural strength is addressed by tolerance factor and octahedral factor. Through the calculation of elastic constants, we have shown that the mechanical stability of all compounds. The PBEsol exchange-correlation potential with the TBmBJ correction was used in this calculation. These perovskites exhibit semiconductor characteristics, with a direct band gap in the (Γ-Γ) direction and an ionic-covalent mixing of chemical bonds and both of these compounds have small direct bandgaps of 1.51 eV and 1.55 eV, the band structure and DOS confirm the semiconducting nature of the material. These materials offer good visible optical absorption and can be employed in optoelectronic applications. Our investigation for the optical, transport, and mechanical properties of both compounds was carried out for the first time as far as we know.

Moreover, these materials have potential for use in the thermoelectric generators due to their extremely low kl values and high ZT. We found a high value (30 %) of SLME at room temperature, which is notable in view of its applications in optoelectronics. Our findings will facilitate highly appropriate construction of lead-free double perovskites and will provide sufficient back-ground to experimental scientists to recognize the potential for energy harvesting.

Data availability statement

Data will be made available on request.

CRediT authorship contribution statement

Anwar ul Haq: Writing – original draft, Investigation, Formal analysis. **Tasawer Shahzad Ahmad:** Methodology. **Afaq Ahmad:** Writing – review & editing, Supervision. **Badriah S. Almutairi:** Writing – review & editing, Resources, Data curation, Conceptualization. **Muhammad Amin:** Investigation, Conceptualization. **M.I. Khan:** Writing – original draft, Data curation. **Nimra Ehsan:** Formal analysis. **Ramesh Sharma:** Resources, Data curation.

Declaration of competing interest

The authors declare that they have no known competing financial interests or personal relationships that could have appeared to influence the work reported in this paper.

Acknowledgement

This research was supported by Princess Nourah bint Abdulrahman University Researchers Supporting Project number (PNURSP2023R327), Princess Nourah bint Abdulrahman University, Riyadh, Saudi Arabia.

References

[1] H. Tang, S. He, C. Peng, A short progress report on high-efficiency perovskite solar cells, Nanoscale Res. Lett. 12 (1) (2017) 1–8, https://doi.org/10.1186/s11671-017-2187-5.
[2] F. Giustino, H.J. Snaith, Toward lead-free perovskite solar cells, ACS Energy Lett. 1 (6) (2016) 1233–1240, https://doi.org/10.1021/acsenergylett.6b00499.
[3] Y. Dang, C. Zhong, G. Zhang, D. Ju, L. Wang, S. Xia, X. Tao, Crystallographic investigations into propertiesf acentric hybrid perovskite single crystals NH (CH3) 3SnX$_3$ (X= Cl, Br), Chem. Mater. 28 (19) (2016) 6968–6974, https://doi.org/10.1021/acs.chemmater.6b02653.
[4] Q. Dong, Y. Fang, Y. Shao, P. Mulligan, J. Qiu, L. Cao, J. Huang, Electron-hole diffusion lengths> 175 μm in solution-grown CH3NH3PbI3 single crystals, Science 347 (6225) (2015) 967–970, https://doi.org/10.1126/science.aaa5760.
[5] C. Lee, J. Hong, A. Stroppa, M.H. Whangbo, J.H. Shim, Organic–inorganic hybrid perovskites ABI 3 (A= CH_3NH_3, NH_2CHNH_2; B= Sn, Pb) as potential thermoelectric materials: a density functional evaluation, RSC Adv. 5 (96) (2015) 78701–78707, https://doi.org/10.1039/C5RA12536G.
[6] T. Zhao, W. Shi, J. Xi, D. Wang, Z. Shuai, Intrinsic and extrinsic charge transport in $CH_3NH_3PbI_3$ perovskites predicted from first-principles, Sci. Rep. 6 (1) (2016) 1–9, https://doi.org/10.1038/srep27327.
[7] S. Choudhary, S. Tomar, D. Kumar, S. Kumar, A.S. Verma, Investigations of lead free halides in Sodium based double perovskites Cs_2NaBiX_6 (X= Cl, Br, I): an ab intio study, East European Journal of Physics (3) (2021) 74–80, https://doi.org/10.26565/2312-4334-2021-3-11.
[8] Z. Xiao, Z. Song, Y. Yan, From lead halide perovskites to lead-free metal halide perovskites and perovskite derivatives, Adv. Mater. 31 (47) (2019), 1803792, https://doi.org/10.1002/adma.201803792.
[9] W.S. Yang, B.W. Park, E.H. Jung, N.J. Jeon, Y.C. Kim, D.U. Lee, S.I. Seok, Iodide management in formamidinium-lead-halide–based perovskite layers for efficient solar cells, Science 356 (6345) (2017) 1376–1379, https://doi.org/10.1126/science.aan2301.
[10] R. Ahmad, G.V. Nutan, D. Singh, G. Gupta, U. Soni, S. Sapra, R. Srivastava, Colloidal lead-free Cs2AgBiBr6 double perovskite nanocrystals: Synthesis, uniform thin-film fabrication, and application in solution-processed solar cells, Nano Res. 14 (4) (2021) 1126–1134, https://doi.org/10.1007/s12274-020-3161-6.
[11] A.U. Haq, G.M. Mustafa, M. Amin, S.M. Ramay, A. Mahmood, Ab-initio study of opto-electronic and thermoelectric properties of direct bandgap double perovskites Rb_2XGaBr_6 (X= Na, K), Int. J. Energy Res. 45 (6) (2021) 9241–9251, https://doi.org/10.1002/er.6455.
[12] T. Leijtens, E.T. Hoke, G. Grancini, D.J. Slotcavage, G.E. Eperon, J.M. Ball, A. Petrozza, Mapping electric field-induced switchable poling and structural degradation in hybrid lead halide perovskite thin films, Adv. Energy Mater. 5 (20) (2015), 1500962, https://doi.org/10.1002/aenm.201500962.
[13] D. Bryant, N. Aristidou, S. Pont, I. Sanchez-Molina, T. Chotchunangatchaval, S. Wheeler, S.A. Haque, Light and oxygen induced degradation limits the operational stability of methylammonium lead triiodide perovskite solar cells, Energy Environ. Sci. 9 (5) (2016) 1655–1660, https://doi.org/10.1039/C6EE00409A.
[14] P.R. Varadwaj, H.M. Marques, Physical and optoelectronic features of lead-free $A_2AgRhBr_6$ (A= Cs, Rb, K, Na, Li) with halide double perovskite composition, J. Mater. Chem. C 8 (37) (2020) 12968–12983, https://doi.org/10.1039/D0TC02501A.
[15] S. Chakraborty, W. Xie, N. Mathews, M. Sherburne, R. Ahuja, M. Asta, S.G. Mhaisalkar, Rational design: a high-throughput computational screening and experimental validation methodology for lead-free and emergent hybrid perovskites, ACS Energy Lett. 2 (4) (2017) 837–845, https://doi.org/10.1021/acsenergylett.7b00035.
[16] A. Jodlowski, A, D. Rodríguez-Padrón, R. Luque, G. de Miguel, Alternative perovskites for photovoltaics, Adv. Energy Mater. 8 (21) (2018), 1703120, https://doi.org/10.1002/aenm.201703120.
[17] F. Giustino, H.J. Snaith, Toward lead-free perovskite solar cells, ACS Energy Lett. 1 (6) (2016) 1233–1240.
[18] M.A. Razzaq, T. Islam, Optoelectronic study of double perovskite Rb2SnBr6: a first principles calculations, Glob. J. Mater. Sci. Eng. 2 (2020) 1–5.
[19] J. Glodo, R. Hawrami, E. Van Loef, W. Higgins, U. Shirwadkar, K.S. Shah, Dual gamma neutron detection with $Cs_2LiLaCl_6$, Hard X-Ray, Gamma-Ray, and Neutron Detector Physics XI 7449 (2009, September) 93–99, https://doi.org/10.1117/12.830127. SPIE.
[20] E.V.D. Van Loef, P. Dorenbos, C.W.E. Van Eijk, K.W. Krämer, H.U. Güdel, Scintillation and spectroscopy of the pure and Ce3+-doped elpasolites: Cs2LiYX6 (X= Cl, Br), J. Phys. Condens. Matter 14 (36) (2002) 8481, https://doi.org/10.1088/0953-8984/14/36/307.
[21] C.W.E. Van Eijk, J.T.M. De Haas, P. Dorenbos, K.W. Kramer, H.U. Gudel, (2005, October). Development of elpasolite and monoclinic thermal neutron scintillators, IEEE Nuclear Science Symposium Conference Record 1 (2005) 239–243, https://doi.org/10.1109/NSSMIC.2005.1596245.
[22] T.I. Al-Muhimeed, J. Alzahrani, S.A. Rouf, S. Al-Qaisi, R. Anbarasan, Q. Mahmood, M. Morsi, Tuning of band gap by anion variation of Ga2TiX6 (X= Cl, Br, I) for solar cells and renewable energy, Phys. Scripta 97 (8) (2022), 085815, https://doi.org/10.1088/1402-4896/ac7efc.

[23] S. Al-Qaisi, M. Mushtaq, J.S. Alzahrani, H. Alkhaldi, Z.A. Alrowaili, H. Rached, M. Morsi, First-principles calculations to investigate electronic, structural, optical, and thermoelectric properties of semiconducting double perovskite Ba2YBiO6, Micro and Nanostructures 170 (2022), 207397, https://doi.org/10.1016/j.micrna.2022.207397.

[24] Y. Li, First-Principles Study of Hybrid Halide Perovskites and beyond for Optoelectronic Applications, University of California, San Diego, 2020.

[25] P. Blaha, K. Schwarz, P. Sorantin, S.B. Trickey, Full-potential, linearized augmented plane wave programs for crystalline systems, Comput. Phys. Commun. 59 (2) (1990) 399–415, https://doi.org/10.1016/0010-4655(90)90187-6.

[26] J.P. Perdew, Density-functional approximation for the correlation energy of the inhomogeneous electron gas, Phys. Rev. B 33 (12) (1986) 8822, https://doi.org/10.1103/PhysRevB.33.8822.

[27] F. Tran, P. Blaha, Accurate band gaps of semiconductors and insulators with a semilocal exchange-correlation potential, Phys. Rev. Lett. 102 (22) (2009), 226401, https://doi.org/10.1103/PhysRevLett.102.226401.

[28] P. Blaha, K. Schwarz, F. Tran, R. Laskowski, G.K. Madsen, L.D. Marks, WIEN2k: an APW+ lo program for calculating the properties of solids, J. Chem. Phys. 152 (7) (2020), 074101, https://doi.org/10.1063/1.5143061.

[29] P. Blaha, K. Schwarz, G.K.H. Madsen, D. Kvasnicka, J. Luitz, An Augmented Plane Wave+ Local Orbital Program for Calculating Crystal Properties, Institut Für Physikalische und Theoretische Chemie, Wien, Austria, 2001, https://doi.org/10.1063/1.5143061.

[30] H. Jiang, Band gaps from the Tran-Blaha modified Becke-Johnson approach: a systematic investigation, J. Chem. Phys. 138 (13) (2013), 134115, https://doi.org/10.1063/1.4798706.

[31] Z. Wu, R.E. Cohen, More accurate generalized gradient approximation for solids, Phys. Rev. B 73 (2006), 235116, https://doi.org/10.1103/PhysRevB.73.235116.

[32] S.Z.A. Shah, S. Niaz, T. Nasir, J. Sifuna, Eco-friendly bismuth based double perovskites X $ _2 $ NaBiCl $ _6 $(X= Cs, Rb, K) for Optoelectronic and Thermoelectric Applications: A First-Principles Study. arXiv preprint arXiv:2208 (2022), 04123, https://doi.org/10.48550/arXiv.2208.04123.

[33] Charles Kittel, Solid State Physics vol. 3, Shell Development Company, 1955.

[34] Q. Mahmood, et al., Optoelectronic and thermoelectric properties of double perovskite Rb2PtX6 (X= Cl, Br) for energy harvesting: first-principles investigations, J. Phys. Chem. Solid. 148 (2021), 109665, https://doi.org/10.1016/j.mtcomm.2022.104083.

[35] J.P. Perdew, K. Burke, M. Ernzerhof, Generalized gradient approximation made simple, Phys. Rev. Lett. 77 (1996) 3865–3868, https://doi.org/10.1103/PhysRevLett.77.3865.

[36] W. Travis, E.N.K. Glover, H. Bronstein, D.O. Scanlon, R.G. Palgrave, On the application of the tolerance factor to inorganic and hybrid halide perovskites: a revised system, Chem. Sci. 7 (7) (2016) 4548–4556, https://doi.org/10.1039/C5SC04845A.

[37] C.J. Bartel, C. Sutton, B.R. Goldsmith, R. Ouyang, C.B. Musgrave, L.M. Ghiringhelli, M. Scheffler, New tolerance factor to predict the stability of perovskite oxides and halides, Sci. Adv. 5 (2) (2019), eaav0693, https://doi.org/10.1126/sciadv.aav0693.

[38] N. Rahman, M. Husain, J. Yang, M. Sajjad, G. Murtaza, M. Ul Haq, A. Khan, First principle study of structural, electronic, optical and mechanical properties of cubic fluoro-perovskites:($CdXF_3$, X= Y, Bi), The European Physical Journal Plus 136 (3) (2021) 1–11, https://doi.org/10.1140/epjp/s13360-021-01177-6.

[39] M.J. Mehl, B.M. Klein, D.A. Papaconstantopoulos, First-principles Calculation of Elastic Properties, Naval Research Lab Washington Dc, 1994.

[40] R. Sa, Y. Wei, W. Zha, D. Liu, A first-principle study of the structural, mechanical, electronic and optical properties of vacancy-ordered double perovskite Cs2TeX6 (X= Cl, Br, I), Chem. Phys. Lett. 754 (2020), 137538, https://doi.org/10.1016/j.cplett.2020.137538.

[41] M. Levy, H. Bass, R. Stern (Eds.), Handbook of Elastic Properties of Solids, Liquids, and Gases, Four-Volume Set, Academic press, 2000.

[42] M. Fox, Optical Properties of Solids, Oxford University Press, 2002.

[43] H. Jones, (1974). Optical Properties of Solids: Frederick Wooten. 260 Pages, Diagrams, Academic Press, Inc., New York, 1972, p. 6× 9.

[44] A. ul Haq, S.S. Iqbal, A. Ahmad, T.S. Ahmad, A. Bakar, S.M. Ramay, Structural stability, mechanical, and optoelectronic properties of A2TlBiI6 (A= Cs and Rb) for energy harvesting: a first principles investigation, J. Phys. Chem. Solid. 111225 (2023), https://doi.org/10.1016/j.jpcs.2023.111225.

[45] P.A. Nawaz, G.M. Mustafa, S.S. Iqbal, N.A. Noor, T.S. Ahmad, A. Mahmood, R. Neffati, Theoretical investigations of optoelectronic and transport properties of Rb2YInX6 (X= Cl, Br, I) double perovskite materials for solar cell applications, Sol. Energy 231 (2022) 586–592, https://doi.org/10.1016/j.solener.2021.11.076.

[46] A.U. Haq, G.M. Mustafa, M. Amin, S.M. Ramay, A. Mahmood, Ab-initio study of opto-electronic and thermoelectric properties of direct bandgap double perovskites Rb2XGaBr6 (X=Na, K), Int. J. Energy Res. 45 (6) (2021) 9241–9251, https://doi.org/10.1002/er.6455.

[47] N. Guechi, A. Bouhemadou, S. Bin-Omran, A. Bourzami, L. Louail, Elastic, optoelectronic and thermoelectric properties of the lead-free halide semiconductors Cs_2AgBiX_6 (X= Cl, Br): ab initio investigation, J. Electron. Mater. 47 (2) (2018) 1533–1545, https://doi.org/10.1007/s11664-017-5962-2.

[48] F. Aslam, B. Sabir, M. Hassan, Structural, electronic, optical, thermoelectric, and transport properties of indium-based double perovskite halides Cs_2InAgX_6 (X= Cl, Br, I) for energy applications, Appl. Phys. A 127 (2) (2021) 1–12, https://doi.org/10.1007/s00339-020-04178-x.

[49] S.A. Mir, D.C. Gupta, Analysis of cage structured halide double perovskites Cs_2NaMCl_6 (M= Ti, V) by spin polarized calculations, J. Alloys Compd. 854 (2021), 156000, https://doi.org/10.1016/j.jallcom.2020.156000.

[50] M. Nabi, D.C. Gupta, Potential lead-free small band gap halide double perovskites Cs_2CuMCl_6 (M= Sb, Bi) for green technology, Sci. Rep. 11 (1) (2021) 1–13, https://doi.org/10.1038/s41598-021-92443-1.

[51] T. Zelai, S.A. Rouf, Q. Mahmood, S. Bouzgarrou, M.A. Amin, A.I. Aljameel, A. Mera, First-principles study of lead-free double perovskites Ga_2PdX_6 (X= Cl, Br, and I) for solar cells and renewable energy, J. Mater. Res. Technol. 16 (2022) 631–639, https://doi.org/10.1016/j.jmrt.2021.12.002.

[52] J. Qian, Y. Liu, J. Song, L. Liu, B. Xu, G. Chen, W. Tian, Spectroscopic Limited Practical Efficiency (SLPE) model for organometal halide perovskites solar cells evaluation, Org. Electron. 59 (2018) 389–398, https://doi.org/10.1016/j.orgel.2018.05.056.

[53] National Renewable Energy Laboratory. (n.d.).Solar Spectral Irradiance Data for AM1.5. U.S. Department of Energy - National Renewable Energy Laboratory. https://www.nrel.gov/grid/solar-resource/spectra-am1.5.html.